National Defence / Défense nationale

UNCLASSIFIED
UNLIMITED DISTRIBUTION

DREV REPORT 4422/86
FILE: 3633B-013
SEPTEMBER 1986

CRDV RAPPORT 4422/86
DOSSIER: 3633B-013
SEPTEMBRE 1986

MULTIPLE-SCATTERING LASER PROPAGATION MODEL AND COMPARISON WITH LABORATORY MEASUREMENTS

L.R. Bissonnette

RESEARCH AND DEVELOPMENT BRANCH
DEPARTMENT OF NATIONAL DEFENCE
CANADA

BUREAU - RECHERCHE ET DÉVELOPPEMENT
MINISTÈRE DE LA DÉFENSE NATIONALE
CANADA

Defence Research Establishment
Centre de recherches pour la Défense
Valcartier, Québec

SANS CLASSIFICATION
DISTRIBUTION ILLIMITÉE

Canada

86-05943/

DREV R-4422/86
FILE: 3633B-013

UNCLASSIFIED

CRDV R-4422/86
DOSSIER: 3633B-013

MULTIPLE-SCATTERING LASER PROPAGATION MODEL AND COMPARISON WITH LABORATORY MEASUREMENTS

by

L.R. Bissonnette

DEFENCE RESEARCH ESTABLISHMENT
CENTRE DE RECHERCHES POUR LA DÉFENSE
VALCARTIER
Tel: (418) 844-4271

Québec, Canada

September/septembre 1986

SANS CLASSIFICATION

ABSTRACT

A multiple-scattering laser propagation model is developed in the form of three simultaneous partial differential equations for the reduced field amplitude, the forward- and the backscattered irradiances. The scattering and diffusion coefficients are defined in terms of Mie functions, and reduction factors are derived to take into account detection at limited fields of view. Solutions for transmitted beam profiles and integrated backscatter are compared with measurements performed on laboratory-generated water droplet clouds at 0.63, 1.06 and 10.6 μm. The agreement is very good for all conditions investigated, ranging from negligible to important multiple-scattering contributions.

RÉSUMÉ

Un modèle de propagation laser en présence de diffusions multiples par des particules en suspension est mis au point sous la forme de trois équations aux dérivées partielles pour l'amplitude réduite du champ, l'intensité lumineuse diffusée vers l'avant et l'intensité lumineuse diffusée vers l'arrière. Les coefficients d'atténuation et de diffusion sont définis au moyen de fonctions de Mie, et des facteurs de réduction sont obtenus pour tenir compte du champ de vue limité des détecteurs. Les solutions du profil des faisceaux transmis et de la rétrodiffusion sont comparées à des mesures faites en laboratoire à 0.63, 1.06 et 10.6 μm sur des nuages de gouttelettes d'eau. L'accord est très bon pour tous les cas étudiés, les contributions des diffusions multiples variant de négligeables à importantes.

TABLE OF CONTENTS

ABSTRACT/RÉSUMÉ 1

1.0 INTRODUCTION 1

2.0 PROPAGATION MODEL 2

3.0 PROPAGATION COEFFICIENTS 5

4.0 SOLUTIONS 8

5.0 FIELD-OF-VIEW EFFECT 11

6.0 COMPARISON WITH MEASUREMENTS 18

6.1 Experiment 18
6.2 Transmitted Beam Profiles 19
6.3 Backscatter 28

7.0 CONCLUSION 37

8.0 REFERENCES 39

FIGURES 1 to 19

TABLE I

1.0 INTRODUCTION

In recent years, many electro-optical systems have been designed to enhance the effectiveness of various military weapons. In clear weather, these systems are very predictive and accurate. However, poor weather conditions and/or artificial obscurants can severely degrade their performance. Thus, a requirement exists for understanding and predicting the propagation of electromagnetic waves under low-visibility conditions created mostly by the presence of natural or man-made aerosols. Also, theoretical developments are needed for the inverse problem of determining the atmospheric optical and infrared parameters from single-ended lidar backscatter measurements.

Propagation in thin or tenuous clouds is well understood and documented (e.g. Refs. 1-2). It is governed by simple and exact single-scattering equations which explain numerous atmospheric phenomena. However, in dense clouds, the single-scattering approximation fails. The optical rays undergo many scattering events before escaping the medium, reaching a target, or being detected. These multiple scatterings have nonnegligible and often dominant effects on the transmitted and backscattered waves. Analytic methods (e.g. Refs. 3-5), transport methods (e.g. Refs. 6-12), and Monte Carlo simulations (e.g. Refs. 13-14) have been used to study this problem. They all constitute very powerful tools, but the mathematics remains complex and no general solutions have been obtained yet.

In a preceding report (Ref. 15), we set the foundations of a multiple-scattering irradiance propagation model based on a stochastic representation of the refractive-index field created by the presence of randomly distributed suspended particles. In the present report, we use the propagation equations derived in Ref. 15 and propose a heuristic but convenient determination of the propagation coefficients. Also, we introduce field-of-view functions to take into account

practical detector geometries. The results are in good agreement with forward- and backscattering measurements in laboratory-generated water droplet clouds.

The propagation equations are given in Chapter 2.0 and the coefficients, in Chapter 3.0. The solutions are derived in Chapter 4.0 and the field-of-view functions, in Chapter 5.0. Chapter 6.0 compares the model predictions with laboratory simulation data.

This work was performed at DREV between April 1985 and January 1986 under PCN 33B13, Multiple-Scattering Effects in Atmospheric Aerosols.

2.0 PROPAGATION MODEL

The model stems from the wave equation of electromagnetic propagation. In the version discussed in this report, we do not consider the polarization effects and we restrict the analysis to one temporal Fourier component of the wave. We thus proceed from the temporal Fourier transform of the scalar wave equation, i.e.

$$\nabla^2 E - \frac{n^2\omega^2}{c^2} E = S, \qquad [1]$$

where E is the Fourier transform of the scalar electric field, ∇^2 is the three-dimensional Laplacian operator, n is the refractive index, ω is the angular frequency of the wave, c is the speed of light in free space, and the right-hand side function S is a source-sink term.

Equation 1 is treated as a stochastic equation since the random spatial, temporal and size distributions of the suspended particles constitute a space-time random field for the complex refractive index n. The statistical properties of the function n can be derived from the number density, shape, size distribution and complex refractive

index of the particles, and the refractive index of the surrounding medium. The model actually postulates two equations similar to eq. 1 to separate the electric field into a forward and a backward wave. The two waves interact through their respective source-sink term S which accounts for the backscatterings from the particles. The formulation of the source-sink terms constitutes a basic feature of the model and is discussed at length in Ref. 15. Here, we only reproduce, with a slight change in notation, the resulting equations for the forward and backward field components E^+ and E^-, i.e.

$$\nabla^2 E^+ - \frac{n^2\omega^2}{c^2} E^+ = ik\, e^{2ikz}\, E^-[\nabla^2\phi_b^- - \nabla^2\phi_b^+], \qquad [2]$$

$$\nabla^2 E^- - \frac{n^2\omega^2}{c^2} E^- = ik\, e^{-2ikz}\, E^+[\nabla^2\phi_b^+ - \nabla^2\phi_b^-], \qquad [3]$$

where $k = n_o\omega/c$ is the wave number in the surrounding medium of index n_o, z is the coordinate along the main direction of propagation, ϕ_b^+ is the random geometrical phase (expressed in units of length) of the wave backscattered from the forward-propagating component E^+, and ϕ_b^- is the random phase of the wave backscattered from the backward-propagating component E^-.

The mechanism of separation of the electromagnetic wave into a forward and a backward component modeled by eqs. 2 and 3 is arbitrary. The original Maxwell's equations contain no such distinction. However, E^+ and E^- constitute a legitimate representation of the total field. One can always rewrite a solution in multiple parts by imposing additional conditions. The condition here is the source-sink function or the right-hand side term in eqs. 2 and 3. This separation is very helpful in practice as it leads to solutions that are experimentally distinguishable.

The stochastic equations 1 and 2 are used to obtain, by standard and straightforward operations, the deterministic equations for the first- and second-order statistical moments of E^+ and E^-, i.e. the average field amplitude and the average irradiance of the forward and backward waves. This produces an unclosed hierarchy of equations since there are more unknowns than equations. The essence of the model consists in the derivation of closure relations to link the higher order unknown moments to the lower order average field amplitude and irradiance functions. This is accomplished through the hypotheses of quasi-homogeneity and quasi-isotropy of the random amplitude and phase functions and of weak but nonnegligible correlation between the instantaneous field amplitude and phase front angle fluctuations. The validity of these assumptions is to be verified a posteriori.

The resulting model equations for the case of a coherent beam directed into a scattering medium are

$$\frac{\partial A}{\partial z} + \frac{r}{z-F}\frac{\partial A}{\partial r} + \frac{A}{z-F} + \frac{1}{2}(\alpha_m + \alpha_a + \alpha_s^+ + \alpha_s^-)A - \frac{i}{2k}\nabla_\perp^2 A = 0, \qquad [4]$$

$$\frac{\partial I^+}{\partial z} + \frac{r}{z-F}\frac{\partial I^+}{\partial r} + \frac{2I^+}{z-F} + (\alpha_m + \alpha_a + \alpha_s^-)\, I^+ - D^+\nabla_\perp^2 I^+ = \alpha_s^+ AA^* + \alpha_s^- I^-, \qquad [5]$$

$$-\frac{\partial I^-}{\partial z} - \frac{r}{z-F}\frac{\partial I^-}{\partial r} - \frac{2I^-}{z-F} + (\alpha_m + \alpha_a + \alpha_s^-)\, I^- - D^-\nabla_\perp^2 I^- = \alpha_s^- AA^* + \alpha_s^- I^+, \qquad [6]$$

i.e. one equation for the forward coherent amplitude A, one for the forward-scattered irradiance I^+, and one for the backscattered irradiance I^-. The coordinate z is the distance along the beam axis, r is the radial coordinate, F is the focal distance and $\nabla_\perp^2$ is the Laplacian operator in the plane normal to the z-axis. The quantities

α_m, α_a, α_s^+, α_s^-, D^+ and D^- are respectively the molecular and aerosol absorption coefficients, the aerosol forward- and backscattering coefficients, and the forward and backward lateral diffusion coefficients.

A simplifying approximation is implicit in eqs. 4-6. The particulate medium was assumed locally homogeneous, i.e. homogeneous over a volume of the size of the beam diameter. This implies that the coefficients α's and D's are functions of the coordinate z only.

3.0 PROPAGATION COEFFICIENTS

The parameters α's and D's of eqs. 4-6 constitute the bulk optical scattering properties of the random medium. They are formally related to the properties of the particles and surrounding medium through the closure relations derived in Ref. 15. Those closure relations are not coupled with the propagation eqs. 4-6. Hence, the problem of determining the α's and D's can be dealt with independently. However, the mathematics is difficult, it requires solving for the covariance function of the geometrical-optics phase front angle fluctuations. That function obeys a three-dimensional nonlinear partial differential equation with coefficient functions of disparate scales. This constitutes a formidable problem which has not been resolved yet.

Since the coefficients α's and D's are independent of the propagation equations, it appears justified to seek a substitute and mathematically more convenient method to determine them. The most suitable candidate is the Mie theory. We therefore propose in this report to define the propagation coefficients heuristically in terms of conventional statistical summations of Mie solutions for single-particle interactions. The method is based on the physical definitions of the coefficients α's and D's.

From simple examination of eq. 4, we find that the coefficients α_m, α_a, α_s^+ and α_s^- model the fading of the incident coherent beam through losses caused by molecular absorption, aerosol absorption, forward- and backscattering. The molecular absorption is assumed known or given. As for the aerosol terms, the descriptions just given are consistent with the standard definitions of aerosol absorption and scattering. Hence, for spherical particles, we set

$$\alpha_s^+ = \int_0^{\pi/2} d\theta \sin\theta \int_0^{2\pi} d\phi \int_0^{\infty} d\rho \frac{dN(\rho)}{d\rho} \pi\rho^2 \frac{dQ_s}{d\Omega}(\theta,\phi,\rho), \qquad [7]$$

$$\alpha_s^- = \int_{\pi/2}^{\pi} d\theta \sin\theta \int_0^{2\pi} d\phi \int_0^{\infty} d\rho \frac{dN(\rho)}{d\rho} \pi\rho^2 \frac{dQ_s}{d\Omega}(\theta,\phi,\rho), \qquad [8]$$

$$\alpha_a = \int_0^{\infty} d\rho \frac{dN(\rho)}{d\rho} \pi\rho^2 Q_e(\rho) - \alpha_s^+ - \alpha_s^- , \qquad [9]$$

where θ is the scattering angle, ϕ is the azimuthal angle, ρ is the particle radius, $dN(\rho)/d\rho$ is the particle size probability density, $dQ_s(\theta,\phi,\rho)/d\Omega$ and $Q_e(\rho)$ are the differential scattering and total extinction efficiencies of a particle of size ρ, and $d\Omega = \sin\theta d\theta d\phi$ is the differential solid angle. The size probability density function is a specified input. The scattering and extinction efficiencies Q_s and Q_e are functions of the radiation wavelength, particle size, and complex refractive indices of the particle and surrounding medium. They are standard expressions of the Mie solutions. Hence, the coefficients α_a, α_s^+ and α_s^- are obtainable through a series of operations well documented in the literature.

The diffusion coefficients D^+ and D^- are modeled as follows:

$$D^{+}(z-z') = (z-z') \frac{\int_0^{2\pi} d\phi \int_0^{\pi/2} d\theta \sin\theta \, p(\theta,\phi)}{\int_0^{2\pi} d\phi \int_0^{\pi/2} d\theta \, p(\theta,\phi)}, \qquad [10]$$

$$D^{-}(z'-z) = (z'-z) \frac{\int_0^{2\pi} d\phi \int_{\pi/2}^{\pi} d\theta \sin\theta \, p(\theta,\phi)}{2\pi \, p(\pi)}, \qquad [11]$$

where $|z-z'|$ is the distance from the point of scattering and $p(\theta,\phi)$ is the phase function defined by

$$p(\theta,\phi) = \frac{1}{(\alpha_s^{+} + \alpha_s^{-})} \int_0^{\infty} d\rho \, \frac{dN(\rho)}{d\rho} \pi\rho^2 \frac{dQ_s}{d\Omega}(\theta,\phi,\rho). \qquad [12]$$

The linear z-dependence is suggested by the asymptotic form of the closure relations of Ref. 15 in the limit of small $|z-z'|$. The proportionality functions are averages of the sine of the scattering angle in the forward and backward hemispheres. The different normalization constants were chosen for best fit with data. Although the formal closure relations indicate that D^{+} and D^{-} should saturate with increasing $|z-z'|$, calculations have shown that the saturation has only marginal effects for the conditions investigated to date.

Equations 7-11 provide a model for calculating the coefficients of the propagation eqs. 4-6. These formulas were obtained by applying the results of the Mie theory to the physical processes represented by the α's and D's. The connection is heuristic but analogous to what is done in the radiative transfer model. Indeed, the radiative transfer equation is a mathematical representation of the scattering phenomenon derived from the conservation of flux. It involves a scattering (or

phase) function which, in practice, is calculated from independent Mie solutions as are the α's and D's of the present model.

4.0 SOLUTIONS

Equations 4-6 constitute a closed system for the solution of the forward and backscattered irradiances resulting from the interaction of a coherent beam with a discrete random medium. The system includes an equation for the amplitude A which yields the reduced irradiance AA^* and two coupled equations for the scattered irradiance functions I^+ and I^-. These differential equations express the rates of change of A, I^+ and I^- due to scattering losses and gains, lateral diffusion and diffraction. The scattering losses are governed by the extinction coefficients. For I^+ and I^-, the extinction coefficient $(\alpha_m + \alpha_a + \alpha_s^-)$ lacks the term α_s^+ compared with that for the reduced irradiance. This means that the forward-scattering process does not constitute a loss to the scattered components of the propagating waves, as expected. The scattering gains or multiple-scattering effects are given by the right-hand side input terms. The reduced irradiance feeds into both the forward- and backscattered irradiances while the counterpropagating scattered waves feed into one another. Finally, the lateral diffraction and diffusion broadenings are modeled by the Laplacian terms of eqs. 4-6. Diffraction also affects the broadening of I^+ and I^-, but it has been left out of eqs. 5 and 6 as beam diffraction is much smaller than lateral diffusion by scattering.

The only difficulty in solving the system of eqs. 4-6 is the coupling between the forward- and backscattered irradiances. Here, we proceed iteratively by first setting $I^- = 0$ in eq. 5 and solving for I^+ and I^- in sequence. Higher order iterations are then obtained by substituting the I^- solution back into eq. 5 and repeating the process. As it turns out, the first iteration is sufficient in many practical

situations. What is neglected is the backscattering of the backscattering.

The iterative solution can easily be obtained in analytic form if the original beam has a Gaussian profile. In this case, the first-iteration solution is

$$AA^*(z,r) = \frac{P_o}{\pi w_o^2} \frac{T(z)}{W(z)} \exp\left[-\frac{r^2}{w_o^2 W(z)}\right], \qquad [13]$$

$$I^+(z,r) = \frac{P_o}{\pi w_o^2} \int_o^z dz' \frac{F(z,z')}{H(z,z')} \exp\left[-\frac{r^2}{w_o^2 H(z,z')}\right], \qquad [14]$$

$$I^-(z,r,Z) = \frac{P_o}{\pi w_o^2} \int_z^Z dz' \frac{G(z,z')}{K(z,z')} \exp\left[-\frac{r^2}{w_o^2 K(z,z')}\right]$$

$$+ \frac{P_o}{\pi w_o^2} \int_z^Z dz' \int_o^{z'} dz'' \frac{L(z,z',z'')}{M(z,z',z'')} \exp\left[-\frac{r^2}{w_o^2 M(z,z',z'')}\right], \qquad [15]$$

where P_o is the beam power, w_o is the beam radius (1/e in irradiance) at the boundary of the cloud ($z = 0$), Z is the depth of the cloud, and z and r are respectively the longitudinal and transversal coordinates of the point of observation. The functions T, F, G and L are "transmittance" functions and W, H, K and M, "beam-spreading" functions. They are given by integrals over the z-coordinate of the propagation coefficients, i.e.

$$T(z) = \exp\left\{-\int_o^z \left[\alpha_m(z') + \alpha_a(z') + \alpha_s^+(z') + \alpha_s^-(z')\right]dz'\right\}, \qquad [16]$$

$$F(z,z') = \alpha_s^+(z')\, T(z')\, \exp\{-\int_{z'}^{z} [\alpha_m(z'') + \alpha_a(z'') + \alpha_s^-(z'')]dz''\}, \quad [17]$$

$$G(z,z') = \alpha_s^-(z')\, T(z')\, \exp\{-\int_{z}^{z'} [\alpha_m(z'') + \alpha_a(z'') + \alpha_s^-(z'')]dz''\}, \quad [18]$$

$$L(z,z',z'') = \alpha_s^-(z')\alpha_s^+(z'')T(z'')\, \exp\{-\int_{z''}^{z'} [\alpha_m(z''') + \alpha_a(z''') + \alpha_s^-(z''')]dz'''\}$$

$$\times \exp\{-\int_{z}^{z'} [\alpha_m(z'') + \alpha_a(z'') + \alpha_s^-(z'')]dz''\}, \quad [19]$$

$$W(z) = \frac{(F-z)^2}{F^2} + \frac{z^2}{k^2 w_o^4}, \quad [20]$$

$$H(z,z') = W(z') + \frac{4}{w_o^2} \int_{z'}^{z} \frac{(z'-F)^2}{(z''-F)^2} D^+(z''-z')dz'', \quad [21]$$

$$K(z,z') = W(z') + \frac{4}{w_o^2} \int_{z}^{z'} \frac{(z'-F)^2}{(z''-F)^2} D^-(z'-z'')dz'', \quad [22]$$

$$M(z,z',z'') = W(z'') + \frac{4}{w_o^2} \int_{z''}^{z'} \frac{(z''-F)^2}{(z'''-F)^2} D^+(z'''-z'')dz'''$$

$$+ \frac{4}{w_o^2} \int_{z}^{z'} \frac{(z'-F)^2}{(z''-F)^2} D^-(z'-z'')dz''. \quad [23]$$

Equations 13-15 give the profiles of the reduced coherent and forward- and backscattered incoherent irradiances resulting from a Gaussian beam directed into an inhomogeneous particulate medium. These solutions account for multiple scatterings of all orders.

5.0 FIELD-OF-VIEW EFFECT

The solutions given by eqs. 13-15 are irradiance solutions and, therefore, applicable to open detectors only. For detection at limited fields of view, the angular distribution of the radiation flux must be taken into account. Here, we model this effect by multiplying the differential contributions to the scattered radiation in eqs. 14 and 15 by a correction factor, as follows:

$$F^{+}(z,r,\Omega_o) = \frac{P_o}{\pi w_o^2} \int_o^z dz' U(z',z,r,\Omega_o) \frac{F(z,z')}{H(z,z')} \exp\left[-\frac{r^2}{w_o^2 H(z,z')}\right], \quad [24]$$

$$F^{-}(z,r,Z,\Omega_o) = \frac{P_o}{\pi w_o^2} \int_z^Z dz' U(z',z,r,\Omega_o) \frac{G(z,z')}{K(z,z')} \exp\left[-\frac{r^2}{w_o^2 K(z,z')}\right]$$

$$+ \frac{P_o}{\pi w_o^2} \int_z^Z dz' V(z',z,r,\Omega_o) \int_o^{z'} dz'' \frac{L(z,z',z'')}{M(z,z',z'')} \exp\left[-\frac{r^2}{w_o^2 M(z,z',z'')}\right], \quad [25]$$

where $F^{+}(z,r,\Omega_o)$ and $F^{-}(z,r,Z,\Omega_o)$ are the forward- and backscattered powers detected within a solid angle Ω_o at point $(z, \underset{\sim}{r})$, and $U(z',z,r,\Omega_o)$ and $V(z',z,r,\Omega_o)$ are field-of-view reduction functions to be specified below. Equation 13 does not need modification since the coherent component conserves its small-divergence characteristics.

The functions U and V are reduction factors which characterize a receiver of field of view Ω_o relative to an open receiver. In other words, U and V in their respective forward- and backscatter configuration measure the fraction of radiation originating from a scattering plane z' and collected by a receiver of field of view Ω_o compared to that collected by an open receiver. U and V are therefore smaller than or equal to unity. In the limit U=1 or V=1, eq. 24 or 25 becomes

identical, by definition, to the original irradiance solution 14 or 15. With reference to Fig. 1 for a schematic definition of the variables, $U(z',z,r,\Omega_o)$ is given by

$$U(z',z,r,\Omega_o) = e^{-\int_{z'}^{z}\alpha_s^+ dz}\left[\frac{\int d^2\underset{\sim}{r}'\ AA^*(z',\underset{\sim}{r}')\ p(z',\theta_s)\ R(\theta_r,\Omega_o)}{\int d^2\underset{\sim}{r}'\ AA^*(z',\underset{\sim}{r}')\ p(z',\theta_s)}\right]$$

$$+\left[1 - e^{-\int_{z'}^{z}\alpha_s^+ dz}\right]\sum_{m=1}^{M}\int dz_1\cdots\int dz_m P(m|z_i)$$

$$\times\left[\frac{\int d^2\underset{\sim}{r}'\int d^2\underset{\sim}{r}_1\cdots\int d^2\underset{\sim}{r}_m R(\theta_r,\Omega_o)AA^*(z',\underset{\sim}{r}')p(z',\theta_o)\prod_{i=1}^{m}p(z_i,\theta_i)}{\int d^2\underset{\sim}{r}'\int d^2\underset{\sim}{r}_1\cdots\int d^2 r_m\ AA^*(z',\underset{\sim}{r}')p(z',\theta_o)\prod_{i=1}^{m}p(z_i,\theta_i)}\right], \quad [26]$$

where p is the phase function, R is the receiver function, the θ's are scattering angles which can be expressed in terms of z, z', z_i, $\underset{\sim}{r}'$ and $\underset{\sim}{r}_i$ by simple trigonometry, $P(m|z_i)$ is the joint probability of a particular configuration z_i of m scattering planes, and M is the maximum number of scattering planes. A similar expression for $V(z', z, r, \Omega_o)$ is obtained by replacing AA^* by Γ^+ in eq. 26.

Equation 26 for U has two main contributions. The first term is the contribution from the radiation that is left unscattered following the primary scattering at z', and the second term is the contribution from the radiation which has experienced at least one scattering between z' and z. For both terms the fraction of detected power is calculated by integrating over all scattering possibilities and ratioing the result for a receiver function $R(\theta_r,\Omega_o)$ to that for an open receiver, i.e. R=1.

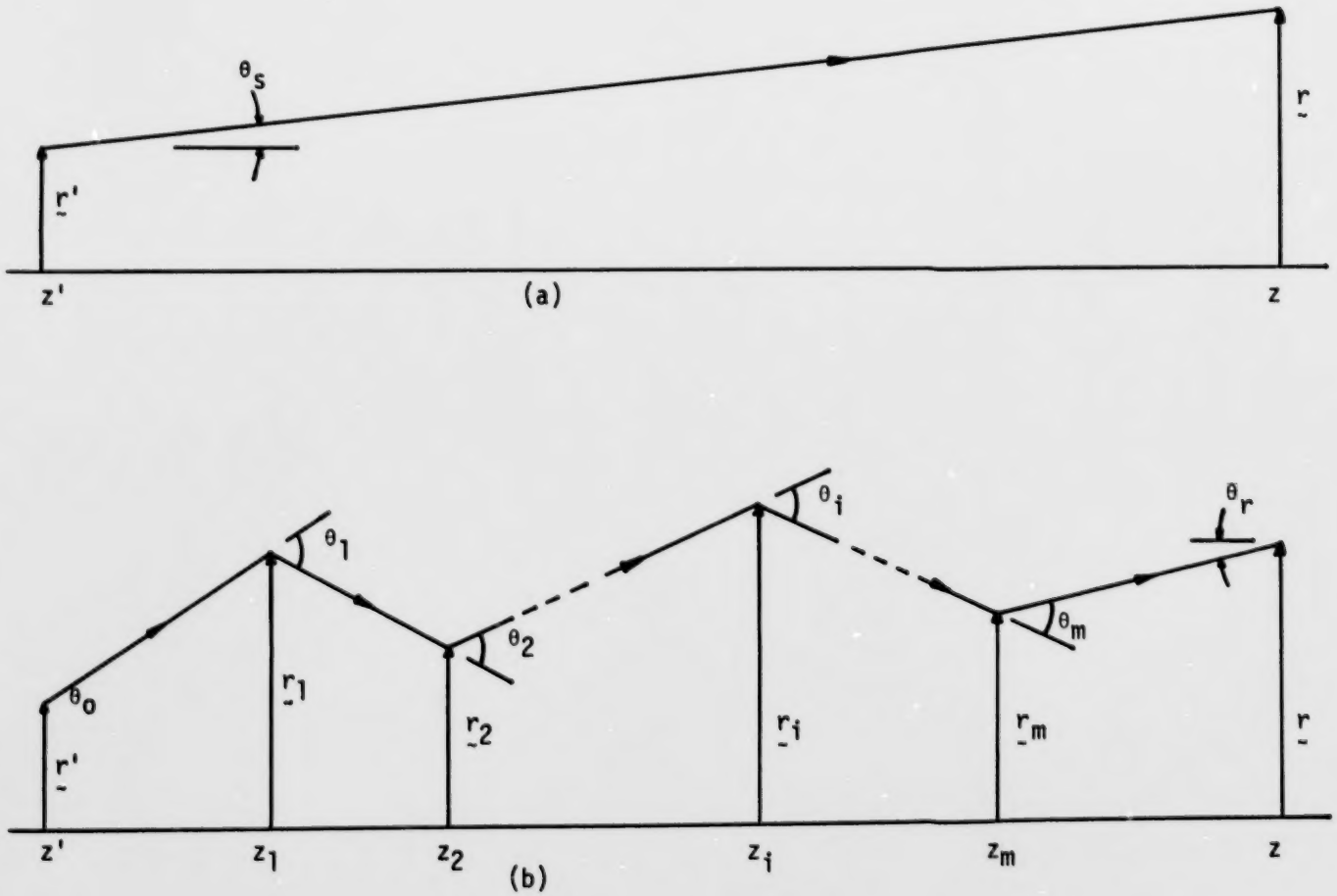

FIGURE 1 - Schematic representation of scattering events for calculating the field-of-view reduction factors U and V. a) single scattering; b) multiple scatterings

The first term of eq. 26 is straightforward. The numerator integral is proportional to the quantity of radiation scattered from plane z' which falls within a field of view of Ω_o at $(z,\underset{\sim}{r})$ after propagating the distance (z-z') without scatterings. The denominator is the corresponding result for an open detector. The second term is more complex but the principle remains the same. The surface integrals give a quantity proportional to the amount of radiation detected at $(z,\underset{\sim}{r})$ after being scattered m times between z' and z, for a receiver function $R(\theta_r,\Omega_o)$ in the numerator and for an open receiver in the denominator. The contributions are summed over all orders of scattering. As indicated by the expressions in the numerator and denominator, the differential scattered radiation reaching the detector is proportional to the product $p(z',\theta_o)\prod_{i=1}^{m} p(z_i,\theta_i)$. At optical and infrared wavelengths and for atmospheric aerosols, the phase functions $p(z_i,\theta_i)$ are peaked in the forward direction. Hence, the resulting integrals decrease rapidly with i for i > 1 unless the θ_i's are near zero. It follows that the ratio of the surface integrals in the last term of eq. 26 is about the same for all values of m. In other words, the m scatterings can be approximated for the purpose of calculating this ratio by a single scattering with non-negligible angle. The ratio can thus be factored out of the summation and since that one scattering can occur with equal probability anywhere between z' and z, we approximate

$$\sum_{m=1}^{M} \int dz_1 \cdots \int dz_m \; P(m|z_i)\; R(z_i) \approx \int_{z'}^{z} \frac{dz_1}{z-z'}\, R(z_1), \qquad [27]$$

where R denotes the ratio of the surface integrals. We thus obtain from eq. 26 the following practical expression to calculate the field-of-view reduction factor U:

$$U(z',z,r,\Omega_o) = e^{-\int_{z'}^{z} \alpha_s^{+} dz} \; \frac{\int d^2\underset{\sim}{r}' AA^*(z',\underset{\sim}{r}')p(z',\theta_s)R(\theta_r,\Omega_o)}{\int d^2\underset{\sim}{r}' AA^*(z',\underset{\sim}{r}')p(z',\theta_s)}$$

$$+\frac{\left[1-e^{-\int_{z'}^{z}\alpha_s^+ dz}\right]}{(z-z')}\int_{z'}^{z}dz_1\left[\frac{\int d^2\underset{\sim}{r}'\int d^2\underset{\sim}{r}_1 R(\theta_r,\Omega_o)AA^*(z',\underset{\sim}{r}')p(z',\theta_o)p(z_1,\theta_1)}{\int d^2\underset{\sim}{r}'\int d^2 r_1 AA^*(z',\underset{\sim}{r}')p(z',\theta_o)p(z_1,\theta_1)}\right] \quad [28]$$

The corresponding factor $V(z',z,r,\Omega_o)$ is obtained by substituting I^+ for AA^*.

Equation 28 completes the method of solution for the forward and backward flux density profiles ($AA^* + F^+$) and F^- for a given receiver geometry. The required inputs are the receiver function $R(\theta_r,\Omega_o)$ and the Mie-derived phase function p and absorption, scattering and diffusion coefficients α's and D's. The reduction factors U and V are calculated by substitution in eq. 28 of the irradiance solutions 13 and 14 for AA^* and I^+. Finally, the required AA^*, F^+ and F^- are obtained from eqs. 13, 24 and 25.

For the general case, the determination of the reduction factors U and V is computation-intensive. However, the surface integrals of eq. 28 can be carried out analytically at considerable savings of computation effort if AA^*, I^+, p and R are approximated by Gaussian functions. Equation 13 shows that this is exactly the case for AA^* while eq. 14 gives I^+ as the sum of Gaussian profiles, which satisfies the condition for analytic integration. The phase function is not Gaussian but the forward peak, which is the dominant contribution here, can be modeled by a Gaussian function with reasonable accuracy. In any case, it is the width of the peak that really matters in the evaluation of U and V and not the exact functional form. Finally, the function $R(\theta_r,\Omega_o)$ of many practical receivers is well represented by a Gaussian. We therefore use the Gaussian approximation to perform the surface integrals of eq. 28 and it is hoped that the ratioing operation will smooth out the differences.

If we let

$$AA^*(z',\underset{\sim}{r}') \text{ or } I^+(z',\underset{\sim}{r}') \sim e^{-r'^2/w^2(z')} \quad [29]$$

$$p(z',\theta_s) \sim e^{-\theta_s^2/\sigma^2(z')}, \quad [30]$$

$$p(z_1,\theta_1) \sim e^{-\theta_1^2/\sigma^2(z_1)}, \quad [31]$$

$$R(\theta_r,\Omega_o) \sim e^{-\theta_r^2/\omega_o^2}, \quad [32]$$

and if we make the paraxial approximation, i.e. the θ's ≤ 0.2, we obtain

$$\frac{\int d^2\underset{\sim}{r}' AA^*(z',\underset{\sim}{r}')p(z',\theta_s)R(\theta_r,\Omega_o)}{\int d^2\underset{\sim}{r}' AA^*(z',\underset{\sim}{r}')p(z',\theta_s)} = \left[\frac{1 + w^2(z')b}{1 + w^2(z')a}\right] \times \exp\left\{\left[\frac{b}{1 + w^2(z')b} - \frac{a}{1 + w^2(z')a}\right]r^2\right\}, \quad [33]$$

$$\frac{\int d^2\underset{\sim}{r}' \int d^2\underset{\sim}{r}_1 AA^*(z',\underset{\sim}{r}')p(z',\theta_s)p(z_1,\theta_1)R(\theta_r,\Omega_o)}{\int d^2\underset{\sim}{r}' \int d^2\underset{\sim}{r}_1 AA^*(z',\underset{\sim}{r}')p(z',\theta_s)p(z_1,\theta_1)} = \left[\frac{dg - f^2}{de - f^2}\right] \times \exp\left\{\frac{c^2f^2(g - e)r^2}{(dg - f^2)(de - f^2)}\right\}, \quad [34]$$

where

$$a = \frac{1}{(z - z')^2}\left\{\frac{1}{\sigma^2(z')} + \frac{1}{\omega_o^2}\right\}, \quad [35]$$

$$b = \frac{1}{(z - z')^2 \sigma^2(z')}, \qquad [36]$$

$$c = \frac{1}{w^2(z')}, \qquad [37]$$

$$d = \frac{1}{w^2(z')} + \frac{1}{(z_1 - z')^2} \left\{ \frac{1}{\sigma^2(z')} + \frac{1}{\sigma^2(z_1)} \right\}, \qquad [38]$$

$$e = \frac{1}{(z_1 - z')^2} \left\{ \frac{1}{\sigma^2(z')} + \frac{(z - z')^2}{(z - z_1)^2} \frac{1}{\sigma^2(z_1)} + \frac{(z_1 - z')^2}{(z - z_1)^2} \frac{1}{\omega_o^2} \right\}, \qquad [39]$$

$$f = \frac{1}{(z_1 - z')^2} \left\{ \frac{1}{\sigma^2(z')} + \frac{(z - z')}{(z - z_1)} \frac{1}{\sigma^2(z_1)} \right\}, \qquad [40]$$

$$g = \frac{1}{(z_1 - z')^2} \left\{ \frac{1}{\sigma^2(z')} + \frac{(z - z')^2}{(z - z_1)^2} \frac{1}{\sigma^2(z_1)} \right\}. \qquad [41]$$

Equations 33 and 34 are substituted in eq. 28 to calculate the reduction factor U or V. The function w^2 is determined from the irradiance solution 13 or 14, σ^2 from the phase function and ω_o^2 is assumed to be given. What remains to be done numerically is the single integration over z_1. It is straightforward to verify that in the limit $\omega_o^2 >> \sigma^2$, i.e. for an open receiver, the factors U and V tend to unity as required.

The model given by eqs. 13, 24 and 25 for the flux density profiles, eqs. 7-11 for the absorption, scattering and diffusion coefficients α's and D's, and eqs. 28, 33 and 34 for the field-of-view reduction factors U and V has been coded for numerical applications. The program calculates the transmitted and backscattered profiles for

specified detectors and propagation media which can be inhomogeneous. The code requires only limited memory space and computation time.

6.0 COMPARISON WITH MEASUREMENTS

6.1 Experiment

For comparison with data, an experiment was designed to measure transmission through and backscatter from well-defined clouds. The most convenient way of achieving reliable control on cloud characteristics is to generate them in an enclosed laboratory environment where the parameters can be varied, monitored and maintained constant. The experiment was carried out by Optech Inc. under contract for DREV (Ref. 16). Water droplet clouds were generated by ultrasonic nebulizers in a chamber of adjustable length. The size distribution of the drops produced by those nebulizers was reasonably invariant. The cloud density was varied by regulating the nebulizers output flow into and out of the chamber. After sufficient settling time and through gentle stirring, a homogeneous concentration was maintained for as long as needed.

The size distribution of the water drops was measured with a Classical Aerosol Scattering Probe (CASP) manufactured by Particle Measuring Systems Inc. and modified for high concentration measurements. The drop diameters were distributed between approximately 0.1 and 15 μm with a peak near 1.0 μm. There are some uncertainties regarding the accuracy of the CASP probe. In particular, it measured more small particles than expected from previous experience. However, as no alternate method of measurement could be explored because of resource constraints, and since the results were reproducible for most cloud densities, the measured distributions were considered representative of the true size distribution of the nebulizer-generated clouds. A typical distribution is illustrated in Fig. 2.

Measurements were performed at three wavelengths: 0.63, 1.06 and 10.6 μm. The extinction coefficient was continuously monitored by recording the cloud transmittance at 0.63 or 1.06 μm. Empirical relations had previously been established between extinction at the three wavelengths of the experiment. Hence, the relevant extinction coefficient could easily be determined from the measured 0.63 or 1.06-μm value. A range of extinction values (at 0.63 μm) between 0 and 3 m^{-1} was covered for a cloud depth of 1.5 or 2.6 m. The remaining parameters necessary for model predictions were determined by Mie calculations based on the size distribution shown in Fig. 2 and the complex refractive index of water at 0.63, 1.06 and 10.6 μm. Table I summarizes the relative parameter values for the conditions of the experiment.

6.2 Transmitted Beam Profiles

The transmitted beam profiles were obtained at the three wavelengths of the experiment. They were measured by scanning a receiver of variable field of view a short distance from the exit window of the cloud chamber. Optical attenuation was used to increase the dynamic range of the detectors, and spurious side-lobe variations were removed by spatially filtering the beam. The unscattered profiles at 0.63, 1.06 and 10.6 μm are shown in Figs. 3-5. As illustrated, the profiles are well approximated by a Gaussian function over about 4 orders of magnitude. Beam diameters at $1/e^2$ in irradiance are respectively 1.15, 0.90 and 1.60 cm for the 0.63, 1.06 and 10.6-μm beams.

The profiles were measured for various extinction coefficients at two fields of view, 20 and 350 mrad, and for two cloud depths, 1.5 and 2.6 m. Figure 6 compares data with model predictions for the 0.63-μm beam, 20 and 350-mrad fields of view, 1.5-m cloud depth, and extinction coefficient of about 3. The agreement is excellent. The

TABLE I

Relative scattering, absorption and diffusion coefficients for the conditions of the Optech experiment (Ref. 16)

λ (μm)	α_s^+/α_e	α_s^-/α_e	α_a/α_e	$D^+/(z-z')$	$D^-/(z'-z)$
0.63	0.956	0.044	0.000	0.040	0.115
1.06	0.949	0.051	0.000	0.065	0.175
10.6	0.396	0.008	0.596	0.285	1.122

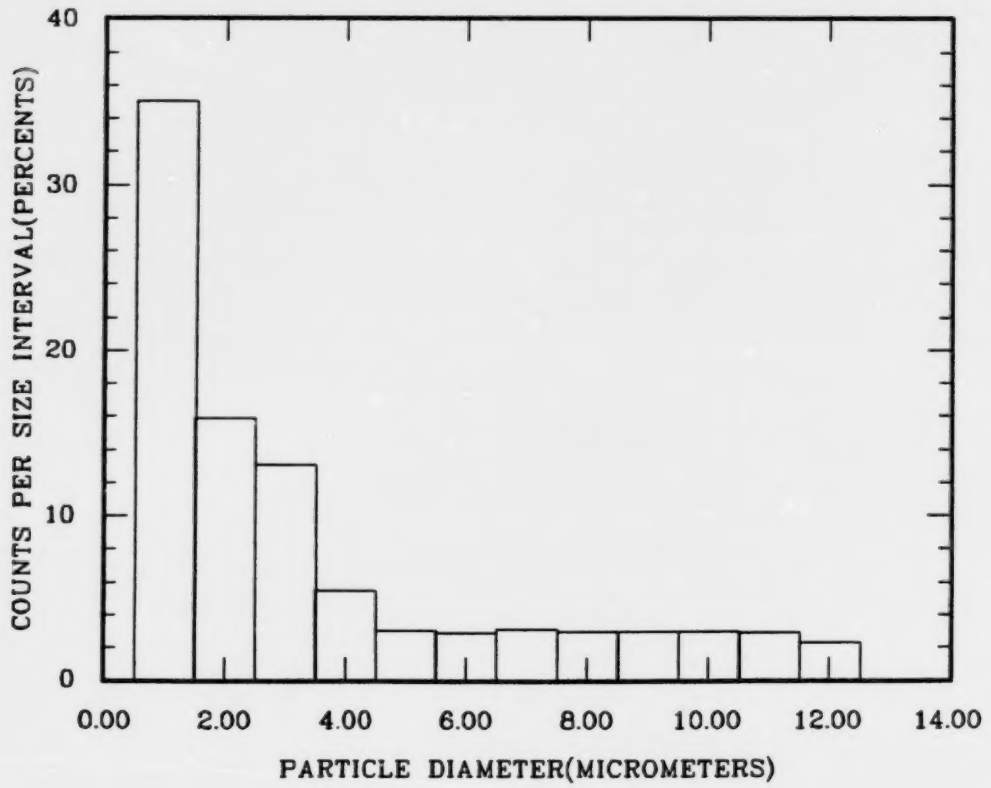

FIGURE 2 - Measured size distribution for nebulizer water droplet clouds

central core of the beam keeps its Gaussian shape and appears unaffected by multiple scatterings. This is the case for both fields of view and it is well confirmed by the model predictions which reveal that the central core consists almost exclusively of the reduced irradiance. Away from the center, the profiles suddenly level off to show the beam-broadening effect caused by multiple scatterings. As illustrated in Fig. 6, the broadening is a function of the receiver field of view. There is a difference of more than 2 orders of magnitude between the off-axis levels recorded at 20 and 350 mrad. The broadened profiles at both 20 and 350 mrad agree very well with the calculated curves. The corresponding results at 1.06 μm are plotted in Fig. 7. The agreement for the 350-mrad data is not as good as in Fig. 6 but is still within expected experimental errors.

The 1.06-μm profile measurements were repeated for a cloud depth of 2.6 m. The results are shown in Fig. 8. The agreement at 350 mrad is good despite some asymmetry in the measured profile, but the calculated off-axis level at 20 mrad is greater than the experimental values by a factor of about 5. It is difficult to explain the origin of this discrepancy, but a slight detector-axis misalignment of the order of 10 mrad with respect to the beam axis could cause a signal drop of this magnitude.

At 10.6 μm, it was very difficult to observe any beam broadening as the forward scattering peak is much wider because of the long wavelength compared with the particle radii. The only conditions that revealed measurable off-axis signal were for a field of view of 350 mrad and a cloud depth of 2.6 m. These data are plotted in Fig. 9 where it is shown that the agreement with the calculated solution is nearly exact.

Figures 10-12 give the transmitted profiles measured with a 350-mrad field of view for various extinction coefficients between 0 and 3. The model solutions are well confirmed in the central core for all conditions illustrated. The solutions of Figs. 10 and 11 show that the off-axis multiscattering level and drop rate are weak functions of the extinction coefficient for the 1.5-m cloud in the range investigated. This is well verified in Fig. 11 for the 1.06-μm beam although the measured values are higher than the model predictions by a factor of about 3. In Fig. 10 for the 0.63-μm beam, there is a non-negligible offset between the off-axis measurements at 0.8 and 1.8 m^{-1} and those at 3.2 m^{-1}. This offset is not borne out by the model but may be explained by experimental errors as the data points show a rather large asymmetry in that case. Finally, the solutions of Fig. 12 for a cloud depth of 2.6 m indicate a greater variation of the off-axis level with extinction coefficient in agreement with the data.

In summary, the transmitted beam profile solutions of the proposed model are well corroborated by the laboratory measurements of Ref. 16. The parameters were varied over a wide range: three wavelengths from the visible at 0.63 μm to the infrared at 10.6 μm; extinction coefficients between 0 and 3 m^{-1} for a cloud depth of 1.5 or 2.6 m which corresponds to optical depths between 0 and 7; and two widely separated receiver fields of view of 20 and 350 mrad. In all cases, the predicted profiles reveal a central core, which retains its Gaussian shape and is essentially the reduced coherent irradiance, flanked by a slowly decreasing flux density level due to forward multiple scatterings. The measured magnitude of this broadened flux density depends strongly on the receiver field of view. Those general features of the solutions are in excellent agreement with the data. There are some discrepancies on the off-axis levels but it cannot be ascertained if they result from experimental or model errors. In any case, there is no trend nor pattern that could point to a systematic flaw in the proposed model.

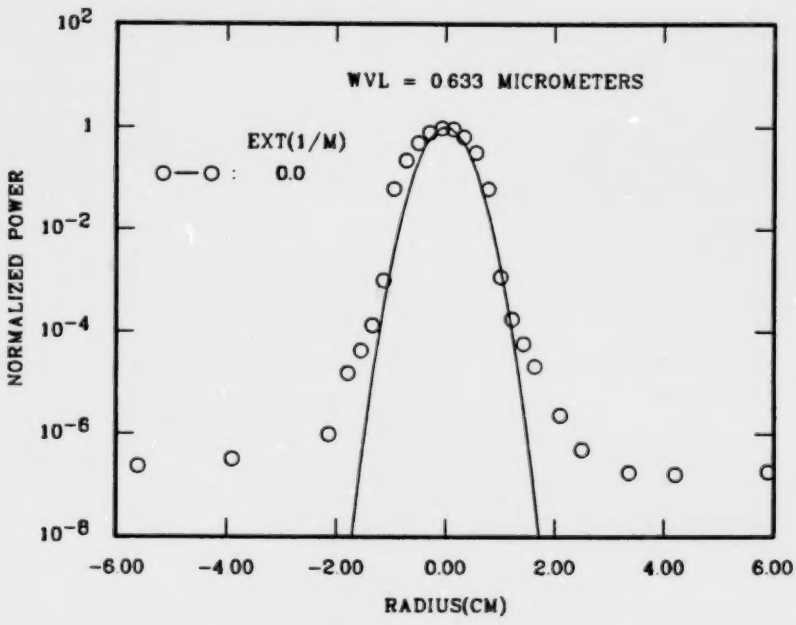

FIGURE 3 - Unattenuated laser beam profile. The symbols are measurements, and the curve is a fitted Gaussian function. The wavelength is 0.63 μm.

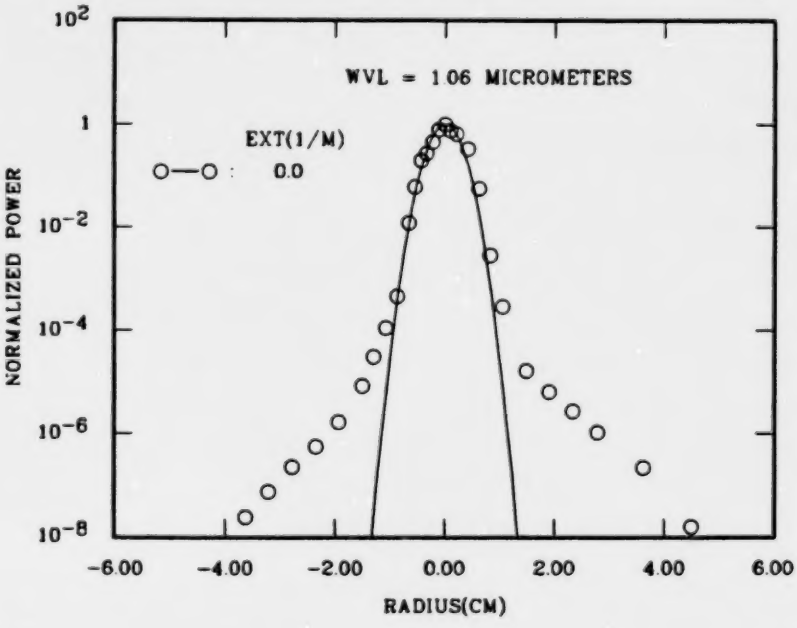

FIGURE 4 - Same as Fig. 3 except that the wavelength is 1.06 μm.

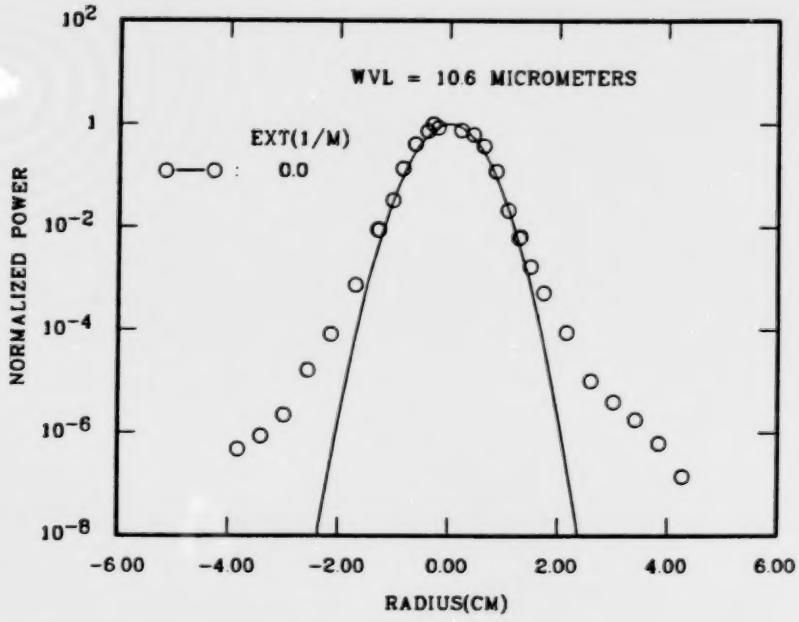

FIGURE 5 - Same as Fig. 3 except that the wavelength is 10.6 μm.

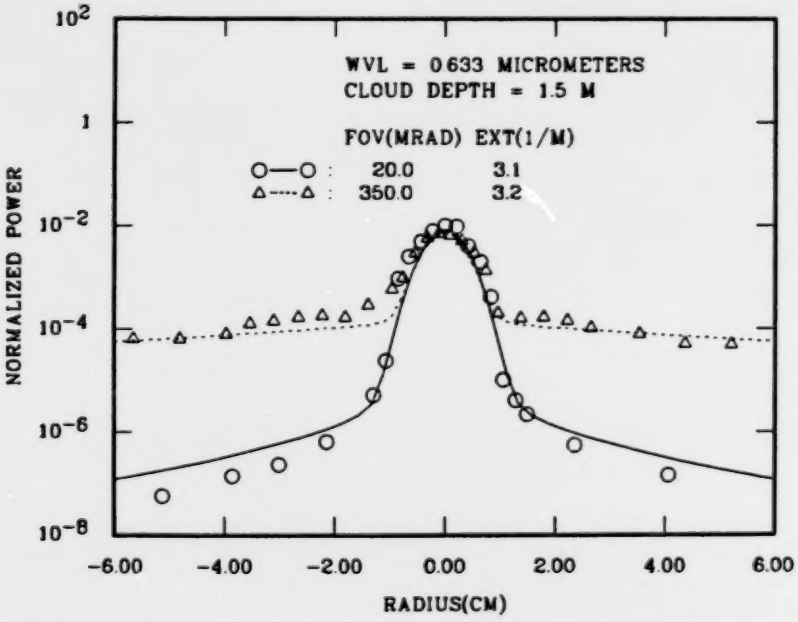

FIGURE 6 - Measured and calculated flux density profiles of a laser beam transmitted through a water droplet cloud as a function of the receiver field of view. The curves are calculations and the symbols, measurements. The wavelength is 0.63 μm and the cloud depth, 1.5 m.

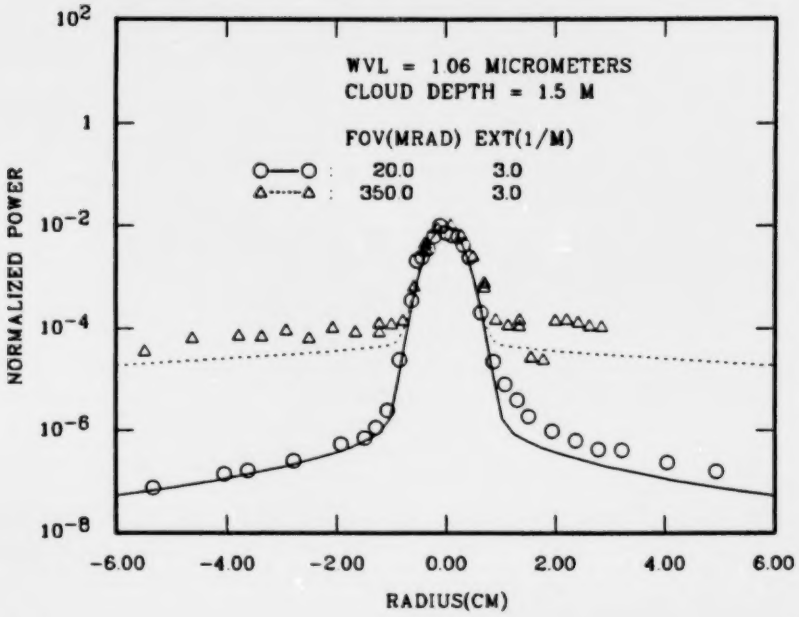

FIGURE 7 - Same as Fig. 6 except that the wavelength is 1.06 μm.

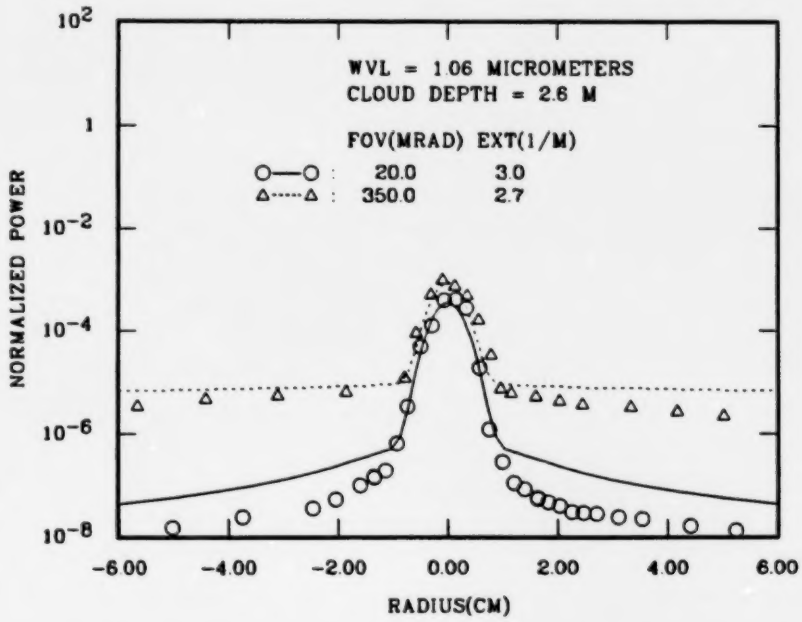

FIGURE 8 - Same as Fig. 7 except that the cloud depth is 2.6 m.

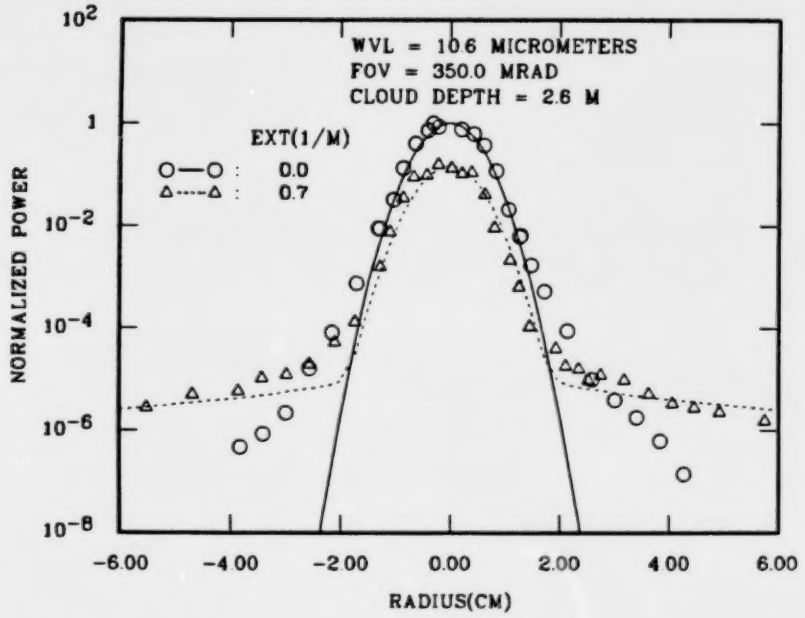

FIGURE 9 - Same as Fig. 8 except that the wavelength is 10.6 μm.

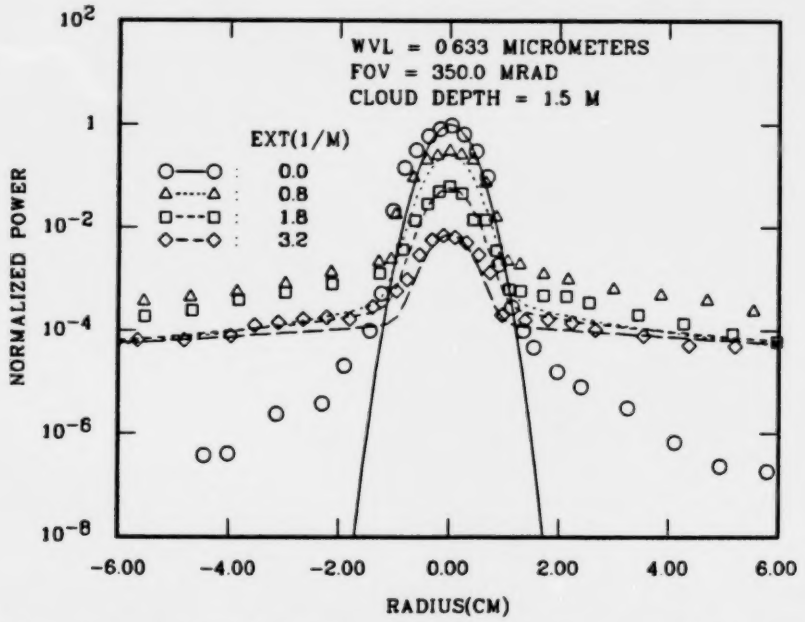

FIGURE 10 - Measured and calculated flux density profiles of a laser beam transmitted through a water droplet cloud as a function of the cloud extinction coefficient. The curves are calculations and the symbols, measurements. The wavelength is 0.63 μm; the cloud depth, 1.5 m; and the receiver field of view, 350 mrad.

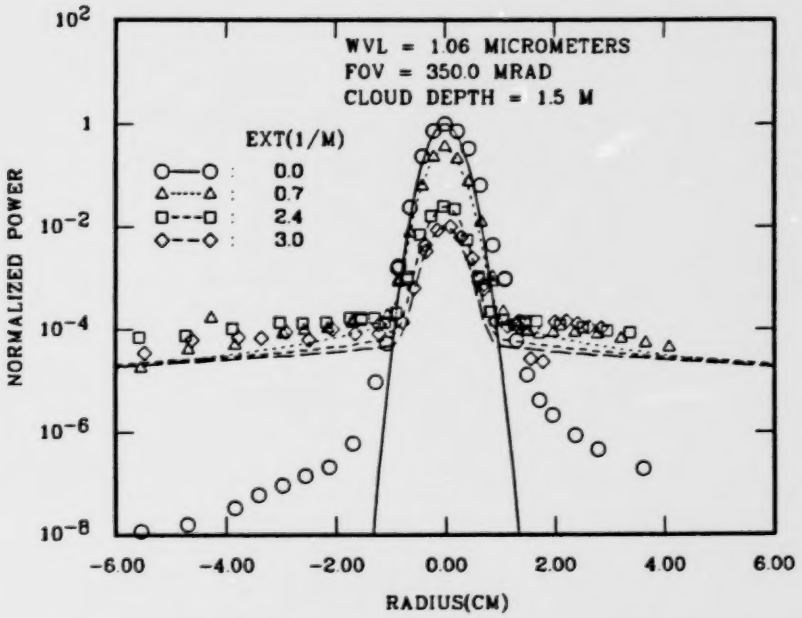

FIGURE 11 - Same as Fig. 10 except that the wavelength is 1.06 μm.

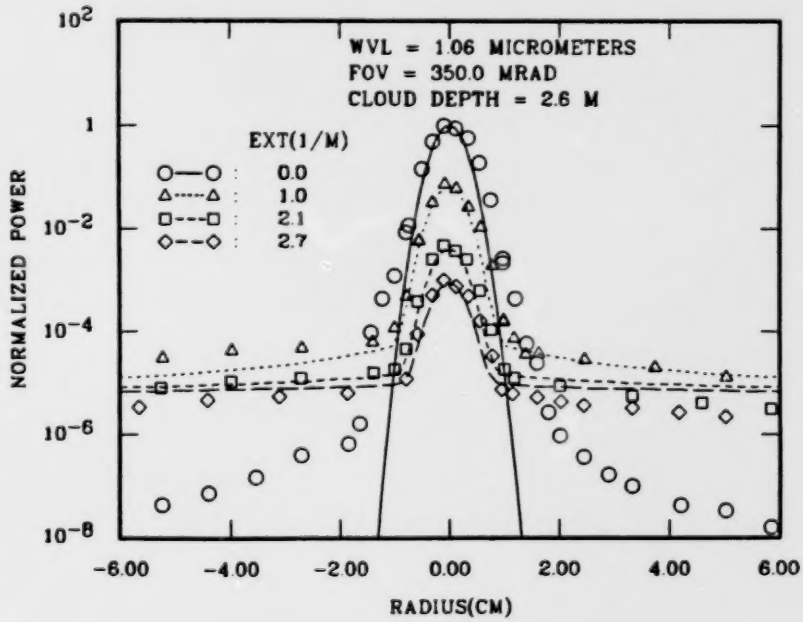

FIGURE 12 - Same as Fig. 11 except that the cloud depth is 2.6 m.

6.3 Backscatter

The lidar technique has great potential as a practical remote sensing device for determining the extinction coefficient of suspended natural and artificial aerosols. However, most existing inversion methods neglect the multiple-scattering contributions, which may have drastic adverse effects on the outcome. The present backscatter solution (eq. 25) could help resolve that problem. Indeed, since eq. 25 is written in analytic form, it can in principle be inverted to retrieve the extinction coefficient from lidar returns affected by multiple scatterings. It is therefore important to validate eq. 25. For that reason, the Optech experiment (Ref. 16) was also designed to generate relevant backscatter data.

The backscatter receiver consisted of a spherical mirror apertured to a 5-cm diameter. The field of view was controlled by a field stop placed in the image plane corresponding to the cloud chamber. Fields of view of 10 and 15 mrad were chosen; 15 mrad is the maximum safe value, given the size of the chamber windows and cloud-to-receiver separation distance. A dichroic beam splitter mounted behind the field stop allowed simultaneous detection at 10.6 μm and either 0.63 or 1.06 μm. The receiver was positioned as close as possible to the laser axis and aligned for total beam overlap over the length of the cloud. The main experiment was conducted for a cloud-to-receiver distance of 10 m but additional tests were made at 8.8 and 5.9 m.

The backscatter returns from the integrated cloud length were measured as functions of wavelength, extinction coefficient, receiver field of view, cloud depth and cloud-to-receiver distance. The cloud return signals were normalized to the signal reflected from a reference Lambertian target placed in front of the chamber window at the beginning of each measurement period. A barium sulfate ($BaSO_4$) target

was used at 0.63 and 1.06 μm and a sanded styrofoam panel at 10.6 μm. A reflectivity of 100% (Ref. 17) is assumed for the barium sulfate, and 35% (Ref. 18) for the styrofoam. The dimensional backscatter can then be calculated by multiplying the normalized data by $P_o r_d^2 \nu / L^2$ where P_o is the laser power, r_d the receiver radius, ν the target reflectivity and L the target-to-receiver distance. However, the reported normalized backscatter results at 0.63 and 1.06 μm are smaller than 1.06-μm data obtained earlier under similar conditions (Ref. 19). A systematic error in the measurement of the reference target return appears to be the cause. Subsequent tests (Ref. 20) performed with two different receivers confirmed that the measured values of Ref. 16 are indeed too small by a multiplicative factor between 2 and 3. To settle the problem, we decided to determine the calibration constant by fitting the measurements in the small-extinction limit to calculations based on the integration of the single-scattering lidar equation, i.e.

$$P(Z) = P_o \frac{S}{Z^2} \beta(\pi,Z) \exp\left\{-2 \int_o^Z \alpha_e(z)dz\right\}, \qquad [42]$$

where P(Z) is the range-resolved lidar return per unit length, Z is the range, P_o is the transmitter power, S is the area of the receiver aperture, $\beta(\pi,Z)$ is the backscatter coefficient, and $\alpha_e(z)$ is the extinction coefficient. This method is acceptable since the single-scattering lidar equation is independent of our propagation model. It has yielded a correction factor of 3.15 for both the 0.63 and 1.06-μm data, which is in reasonable agreement with the correction estimated from the post-experiment tests.

The backscatter measurements at 0.63 μm for the 1.5-m cloud, 10-m cloud-to-receiver distance and 10 and 15-mrad fields of view are compared with the model predictions in Fig. 13. The agreement is almost exact except for the 15-mrad case where the theoretical solution is about 5% higher than the data at high extinction values. These

small differences are well within the experimental uncertainties especially since the field-of-view functions were not directly measured but inferred from the field-stop sizes. The solution obtained by integrating the single-scattering lidar equation is also drawn for comparison. It is in perfect agreement with the present solutions for extinction values smaller than about 0.3 m^{-1} at which point it begins to saturate while the measured returns and multiple-scattering solutions continue to grow, although at a gradually slower rate. These results show that the multiple-scattering effects indicated by the field-of-view dependence and larger backscatter signal are very important for the conditions of Fig. 13 and well accounted for by the present model.

The corresponding results obtained at 1.06 μm are plotted in Fig. 14. The fit is not as close as in Fig. 13 but still within acceptable limits. The multiple-scattering effects are less than those at 0.63 μm, which is in agreement with the predictions. In particular, the measured field-of-view differences are not as explicit as in Fig. 13, but it must be noted that there is only one set of data at 15 mrad for three independent sets at 10 mrad. Thus, the 10-mrad experimental scatter resulting from measurements on different occasions may be responsible for confusing the field-of-view discrimination. There is a slight change in the data slope at an extinction value of about 1.5 m^{-1}. It could not be determined if this change is real or is an artifact of the experiment.

The results obtained at 10.6-μm are plotted in Fig. 15. As it turns out, the water clouds are much less efficient scatterers at 10.6 μm than at 0.63 or 1.06 μm; the returns are smaller by about 2 orders of magnitude. This explains the larger experimental scatter of the experimental values of Fig. 15 compared with those of Fig. 13 or 14. Within that scatter, the low-extinction half of the data agrees very well with the model solutions. However, there is a sudden increase

near the extinction value of 0.4 m^{-1} which is not borne out by the solutions. This effect is probably artificial and due to reflections of forward-scattered radiation off chamber walls (Ref. 20). On the other hand, there is very good agreement on the weak field-of-view dependence between the 10 and 15-mrad receivers. This weak dependence results from the wide angular forward scattering demonstrated by the theoretical and experimental results given in Fig. 9. In other words, there are very few multiple-scattering contributions within fields of view of the order of 10-15 mrad. This is further corroborated by the fact (illustrated in Fig. 15) that the single-scattering solution is only slightly less than the present solutions for 10 and 15 mrad.

The cloud depth effect was also investigated. The results for a cloud depth of 2.6 m are reproduced in Figs. 16 for 1.06 μm and 17 for 10.6 μm. The cloud-to-receiver distance was reduced to 8.8 m. The measurements at 1.06 μm fit the solution very well in the limit of small extinction coefficients, but they suddenly change slope at about 0.4 m^{-1} to fall below the theoretical curve although they remain approximately parallel to it thereafter. The differences are of the order of 20-30%. No exact explanation could be found but it is most likely an experimental error since the high-extinction returns for this case are nearly equal to (or even smaller than) those of Fig. 14 for a smaller cloud depth and greater cloud-to-receiver distance. The corresponding results at 10.6 μm shown in Fig. 17 follow approximately the same pattern as for the 1.5-m cloud (Fig. 15). There is a fair agreement at the small-extinction end, but the calculations are smaller than the data by about 30% following the sudden increase of the measurements near 0.4 m^{-1}. As in Figure 15, the same explanation of contamination by wall reflections is probably applicable.

The influence of the cloud-to-receiver distance was studied by moving the 2.6-m chamber closer to the receiver, from 8.8 to 5.9 m. Measurements in that case were complicated by the shorter separation

and longer cloud length, which made it more difficult to adjust for proper overlap and caused uncertainties in the field-of-view definition since the depth of focus could not accommodate the whole length of the cloud. The results are plotted in Figs. 18 for 1.06 μm and 19 for 10.6 μm. In both cases, the agreement is good at small extinction coefficients but the subsequent rise of backscatter with extinction coefficient is faster than predicted. At 10.6 μm, this appears to be the same behavior as in Fig. 17 for 8.8-m distance except that it is amplified. At 1.06 μm, the experimental slope is now greater than that of the theoretical curve. There are no clear explanations for these effects but a probable cause may be related to the overlap and depth-of-focus problems discussed above. If indeed present, these translate into a range-dependent field of view which is not accounted for by the fixed function used for the calculations.

In summary, the backscatter solutions of the proposed model are wel' validated by the laboratory data of Ref. 16. The basic results given in Figs. 13-15 for the 1.5-m cloud demonstrate an agreement of better than 10% for the three wavelengths and the two fields of view except for the high-extinction measurements at 10.6 μm which are probably contaminated by wall reflections. The data of Figs. 13-15 are the more reliable of the series since the 1.5-m cloud/10-m cloud-to-receiver separation constitutes the primary configuration of the Optech experiment which has been extensively tested. The additional data with the 2.6-m cloud and separation distance of 8.8 and 5.9 m are probably affected by depth-of-focus and overlap problems. There are obvious errors such as the smaller returns at 8.8 m than at 10.0 m or the larger-than- expected returns for high extinction coefficients at 10.6 μm. Considering these effects, the theoretical fits of Figs. 16-19 appear reasonable. Moreover, the solutions of Figs. 16-19 exhibit features easily explained by simple physical arguments. First, there is the overall increase of the signal level with a decrease of the cloud-to-receiver separation which is simply the geometric-range

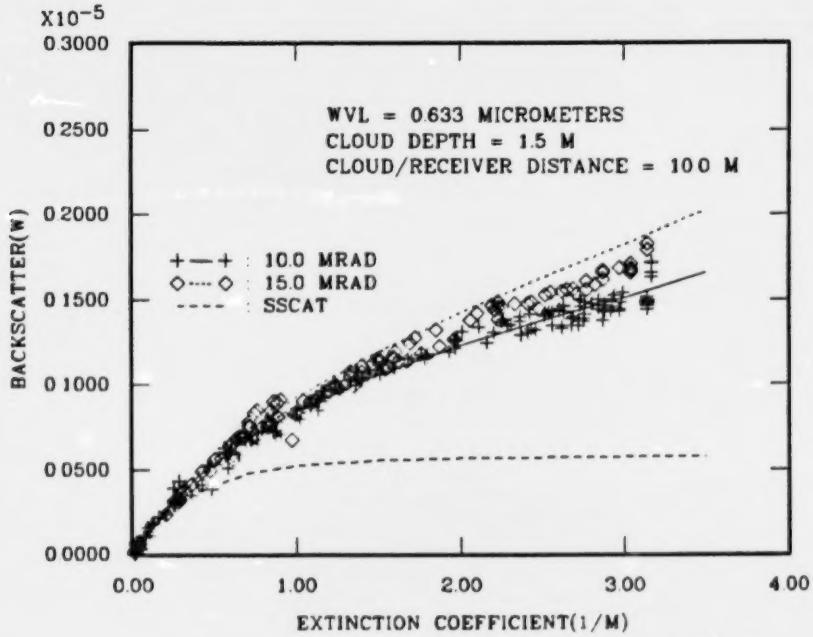

FIGURE 13 - Measured and calculated backscattered power from a water droplet cloud as a function of the cloud extinction coefficient and receiver field of view. The curves are calculations and the symbols, measurements. SSCAT is single-scattering solution. The wavelength is 0.63 μm; the cloud depth, 1.5 m; and the cloud-to-receiver separation, 10 m.

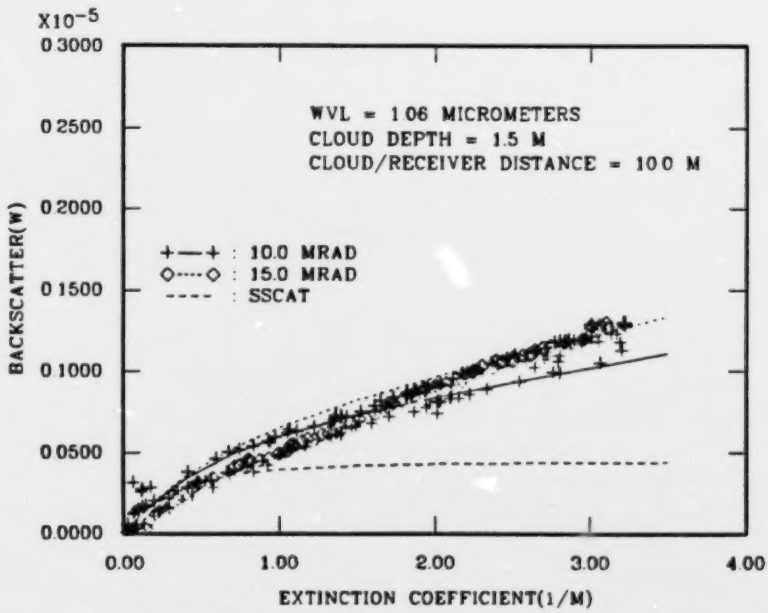

FIGURE 14 - Same as Fig. 13 except that the wavelength is 1.06 μm.

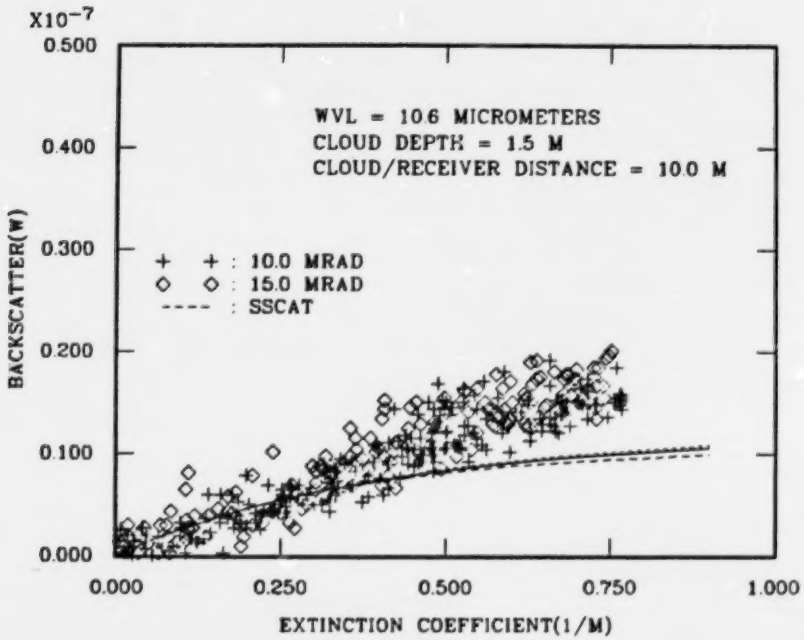

FIGURE 15 - Same as Fig. 13 except that the wavelength is 10.6 μm.

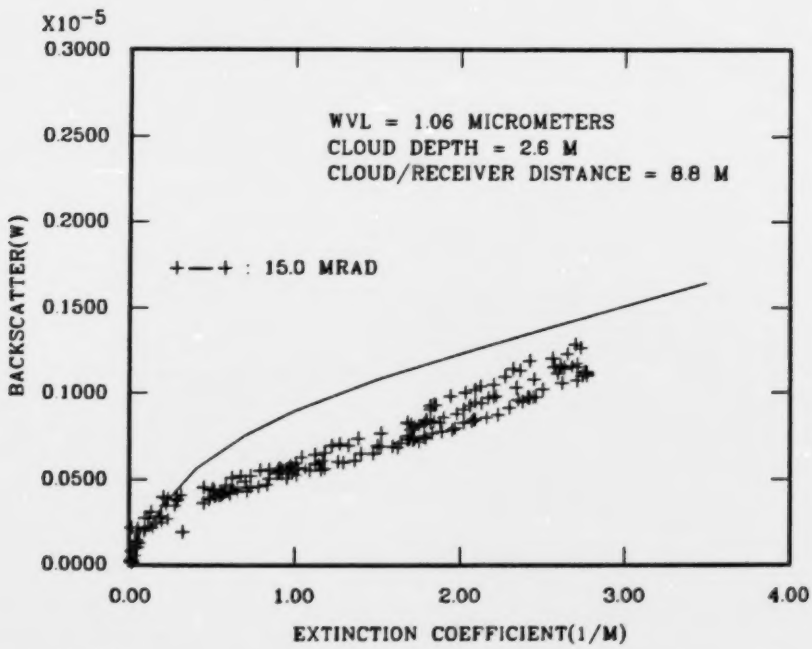

FIGURE 16 - Same as Fig. 14 except that the cloud depth is 2.6 m and the cloud-to-receiver separation, 8.8 m.

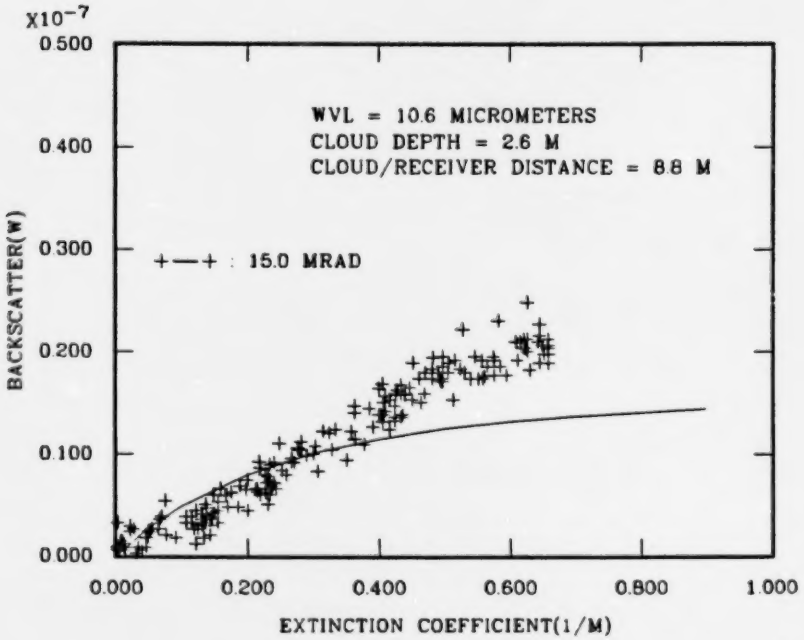

FIGURE 17 - Same as Fig. 16 except that the wavelength is 10.6 μm.

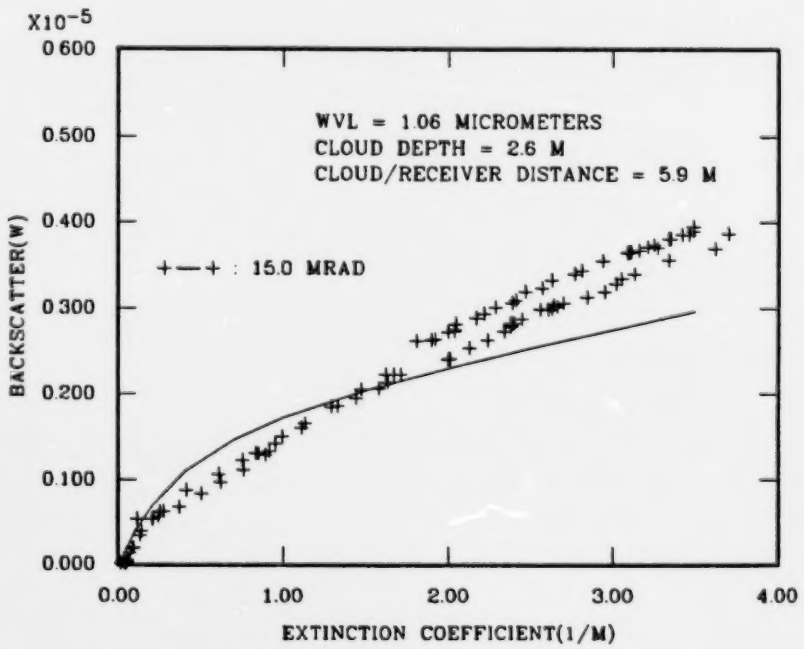

FIGURE 18 - Same as Fig. 14 except that the cloud depth is 2.6 m and the cloud-to-receiver separation, 5.9 m.

factor. Second, there is the steeper slope at small extinction coefficients for larger cloud depths. This occurs because at small extinction the backscatter from the entire length of the cloud, even for an extended depth, contributes to the detection; whereas at high extinction the backscatter from the far end is more attenuated if the cloud is longer. Thus, the backscatter is proportional to cloud length in the low-extinction limit but gradually becomes independent of it as the extinction grows. This explains, in agreement with the present model, why the integrated backscatter initially increases faster for greater cloud depths.

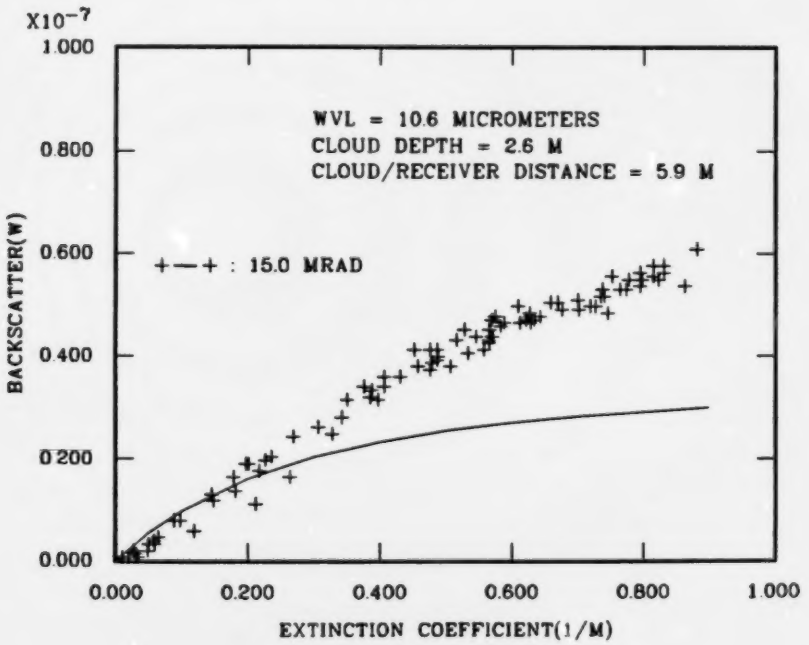

FIGURE 19 - Same as Fig. 18 except that the wavelength is 10.6 μm.

7.0 CONCLUSION

The proposed multiple-scattering propagation model is well validated by the laboratory simulation data of Ref. 16. The predicted flux density profiles of the transmitted radiation show a central core surrounded by a low-level and much more uniform flux distribution. These features were well verified over the complete parameter range investigated which included three wavelengths, two receiver fields of view, and optical depths between 0 and approximately 7. The discrepancies between measured and predicted off-axis levels show no particular trend and are within expected measurement errors.

The backscatter solutions are in excellent agreement with the basic 1.5-m cloud data for three wavelengths, two fields of view, and optical depths between 0 and 4.5. For the larger 2.6-m cloud and shorter cloud-to-receiver separations which stretch to the limit the designed receiver specifications, there are differences of 20 to 100%. However, considering all possible causes of experimental errors, the fit is acceptable. The solutions are found to adjust to the greater cloud depth and shorter separation in ways consistent with simple physical explanations, in particular, the more rapid rise of backscatter at small extinction coefficients and the overall increase in the signal level.

A complementary test was performed by comparing the backscatter solutions of the present model with Monte Carlo calculations (Ref. 21). The computations were carried out for a 1-km-deep cloud and a cloud-to-receiver separation of 200 m. Three wavelengths (1.06, 3.5 and 10.5 μm), six cloud models (maritime aerosols 70 and 99% RH, rural aerosols 70 and 99% RH, and urban aerosols 70 and 99% RH; Ref. 22), three extinction coefficients (0.5, 2.0 and 5.0 km^{-1}), and two fields of view (1 and 10°) were investigated. For each case, the ratio of the Monte Carlo to the present model backscatter returns was calculated. The

resulting average ratio is 1.01 with a standard deviation of 0.05, and the maximum and minimum values are 1.10 and 0.75 respectively. Therefore, the agreement between the two different solution methods is excellent and provides further corroboration for the proposed model on a scale representative of atmospheric applications.

The results of this report show that the model defined by the propagation eqs. 4-6, the parameter definitions 7-11, and the field-of-view functions U and V of eq. 28 is a valid representation of the multiple-scattering effects on laser propagation and scattering in aerosol clouds. Forward- and backscattering phenomena at optical and infrared wavelengths in aerosols of extinction coefficients as high as 3 m^{-1} were properly modeled. This constitutes a posteriori confirmation of the hypotheses leading to the propagation eqs. 4-6 and of the heuristic determination of the scattering and diffusion coefficients α's and D's. The solutions are given by analytic expressions, eqs. 13-23, which handle inhomogeneous clouds, are easily coded, and require reasonable computation efforts. Backscatter calculations are faster than with the biased Monte Carlo code of Ref. 21 by a factor of at least 20. Since the solutions are analytic, they are, in principle, applicable to the inverse lidar problem in the presence of multiple-scattering contributions. This is an interesting property that will be investigated in future work.

8.0 REFERENCES

1. Ishimaru, A., "Wave Propagation and Scattering in Random Media", Vols. 1 and 2, Academic Press, New York, 1978.

2. Zuev, V.E., "Laser Beams in the Atmosphere", translated from Russian by James S. Wood, Consultants Bureau, Plenum Publishing Corp., 1982.

3. Twersky, V., "Interference Effects in Multiple Scattering by Large, Low-Refracting, Absorbing Particles", J. Opt. Soc. Am., Vol. 60, pp. 908-914, 1970.

4. Twersky, V., "Absorption and Multiple Scattering by Biological Suspensions", J. Opt. Soc. Am., Vol. 60, pp. 1084-1093, 1970.

5. Twersky, V., "Multiple Scattering of Sound by a Periodic Line of Obstacles", J. Acoust. Soc. Am., Vol. 53, No. 1, pp. 96-112, 1973.

6. Arnush, D., "Underwater Light Beam Propagation in the Small-Angle-Scattering Approximation", J. Opt. Soc. Am., Vol. 62, pp. 1109-1111, 1972.

7. Fante, R.L., "Propagation of Electromagnetic Waves Through Turbulent Plasma Using Transport Theory", IEEE Trans Antennas Propag., AP-21, pp. 750-755, 1973.

8. Hong, S.T. and Ishimaru, A., "Two-Frequency Mutual Coherence Function; Coherence Bandwidth; and Coherence Time of Millimeter and Optical Waves in Rain, Fog and Turbulence", Radio Sci., Vol. 11, pp. 551-559, 1976.

9. Stotts, L.B., "The Radiance Produced by Laser Radiation Transversing a Particulate Multiple-Scattering Medium", J. Opt. Soc. Am., Vol. 67, pp. 815-819, 1977.

10. Tam, W.G. and Zardecki, A., "Multiple Scattering of a Laser Beam by Radiational and Advective Fogs", Optica Acta, Vol. 26, pp. 659-670, 1979.

11. Box, M.A. and Deepak, A., "Limiting Cases of the Small-Angle Scattering Approximation Solutions for the Propagation of Laser Beams in Anisotropic Scattering Media", J. Opt. Soc. Am., Vol. 71, pp. 1534-1539, 1981.

12. Ishimaru, A., Kuga, Y., Cheung, R.L.-T. and Shimizu, K., "Scattering and Diffusion of a Beam Wave in Randomly Distributed Scatterers", J. Opt. Soc. Am., Vol. 73, pp. 131-136, 1983.

13. Plass, G.N. and Kattawar, G.W., "Monte Carlo Calculations of Light Scattering from Clouds", Appl. Opt., Vol. 7, pp. 415-419, 1968.

14. Bucher, E.A., "Computer Simulation of Light Pulse Propagation for Communication through Thick Clouds", Appl. Opt., Vol. 12, pp. 2391-2400, 1973.

15. Bissonnette, L.R., "Laser Forward- and Backscattering in Particulate Media", DREV R-4351/85, March 1985, UNCLASSIFIED

16. Smith, R.B., Houston, J.D., Ulitsky, A., Carswell, A.I. and Sutherland, P.B., "Propagation and Scattering in Atmospheric Aerosols", Optech Inc. Report No. IR0672 prepared for Defence Research Establishment Valcartier, Contract #14SD.97701-3-82227, July 1985, UNCLASSIFIED

17. Grum, F. and Luckey, G.W., "Optical Sphere Paint and a Working Standard of Reflectance", Appl. Opt., Vol. 7, pp. 2289-2294, 1968.

18. Henshall, H. and Cruickshank, J., Defence Research Establishment Valcartier, Private communication.

19. Smith, R.B., Carswell, A.I., Houston, J.D., Pal, S.R. and Greiner, B.C., "Multiple Scattering Effects on Backscattering and Propagation of Infrared Laser Beams in Dense Military Screening Clouds", Optech Inc. report prepared for Defence Research Establishment Valcartier, Contract #09SD.97701-0-66254, February 1983, UNCLASSIFIED

20. Smith, R.B., Optech Inc., Private communication.

21. Duncan, L.D. and Shirkey, R.C., "EOSAEL 82 - A Library of Battlefield Obscuration Models", Optical Engineering, Vol. 22, pp. 20-23, 1983.

22. Shettle, E.P. and Fenn, R.W., "Models for the Aerosols of the Lower Atmosphere and the Effects of Humidity Variations on their Optical Properties", AFGL-TR-79-0214, Air Force Geophysics Laboratory, Hanscom AFB, Massachusetts, September 1979, UNCLASSIFIED

CRDV R-4422/86 (SANS CLASSIFICATION)

Bureau - Recherche et Développement, MDN, Canada.
CRDV, C.P. 8800, Courcelette, Qué. G0A 1R0

"Modèle de propagation laser en présence de diffusions multiples et comparaison avec des mesures prises en laboratoire"
par L.R. Bissonnette

Un modèle de propagation laser en présence de diffusions multiples par des particules en suspension est mis au point sous la forme de trois équations aux dérivées partielles pour l'amplitude réduite du champ, l'intensité lumineuse diffusée vers l'avant et l'intensité lumineuse diffusée vers l'arrière. Les coefficients d'atténuation et de diffusion sont définis au moyen de fonctions de Mie, et des facteurs de réduction sont obtenus pour tenir compte du champ de vue limité des détecteurs. Les solutions du profil des faisceaux transmis et de la rétrodiffusion sont comparées à des mesures faites en laboratoire à 0.63, 1.06 et 10.6 μm sur des nuages de gouttelettes d'eau. L'accord est très bon pour tous les cas étudiés, les contributions des diffusions multiples variant de négligeables à importantes.

CRDV R-4422/86 (SANS CLASSIFICATION)

Bureau - Recherche et Développement, MDN, Canada.
CRDV, C.P. 8800, Courcelette, Qué. G0A 1R0

"Modèle de propagation laser en présence de diffusions multiples et comparaison avec des mesures prises en laboratoire"
par L.R. Bissonnette

Un modèle de propagation laser en présence de diffusions multiples par des particules en suspension est mis au point sous la forme de trois équations aux dérivées partielles pour l'amplitude réduite du champ, l'intensité lumineuse diffusée vers l'avant et l'intensité lumineuse diffusée vers l'arrière. Les coefficients d'atténuation et de diffusion sont définis au moyen de fonctions de Mie, et des facteurs de réduction sont obtenus pour tenir compte du champ de vue limité des détecteurs. Les solutions du profil des faisceaux transmis et de la rétrodiffusion sont comparées à des mesures faites en laboratoire à 0.63, 1.06 et 10.6 μm sur des nuages de gouttelettes d'eau. L'accord est très bon pour tous les cas étudiés, les contributions des diffusions multiples variant de négligeables à importantes.

CRDV R-4422/86 (SANS CLASSIFICATION)

Bureau - Recherche et Développement, MDN, Canada.
CRDV, C.P. 8800, Courcelette, Qué. G0A 1R0

"Modèle de propagation laser en présence de diffusions multiples et comparaison avec des mesures prises en laboratoire"
par L.R. Bissonnette

Un modèle de propagation laser en présence de diffusions multiples par des particules en suspension est mis au point sous la forme de trois équations aux dérivées partielles pour l'amplitude réduite du champ, l'intensité lumineuse diffusée vers l'avant et l'intensité lumineuse diffusée vers l'arrière. Les coefficients d'atténuation et de diffusion sont définis au moyen de fonctions de Mie, et des facteurs de réduction sont obtenus pour tenir compte du champ de vue limité des détecteurs. Les solutions du profil des faisceaux transmis et de la rétrodiffusion sont comparées à des mesures faites en laboratoire à 0.63, 1.06 et 10.6 μm sur des nuages de gouttelettes d'eau. L'accord est très bon pour tous les cas étudiés, les contributions des diffusions multiples variant de négligeables à importantes.

CRDV R-4422/86 (SANS CLASSIFICATION)

Bureau - Recherche et Développement, MDN, Canada.
CRDV, C.P. 8800, Courcelette, Qué. G0A 1R0

"Modèle de propagation laser en présence de diffusions multiples et comparaison avec des mesures prises en laboratoire"
par L.R. Bissonnette

Un modèle de propagation laser en présence de diffusions multiples par des particules en suspension est mis au point sous la forme de trois équations aux dérivées partielles pour l'amplitude réduite du champ, l'intensité lumineuse diffusée vers l'avant et l'intensité lumineuse diffusée vers l'arrière. Les coefficients d'atténuation et de diffusion sont définis au moyen de fonctions de Mie, et des facteurs de réduction sont obtenus pour tenir compte du champ de vue limité des détecteurs. Les solutions du profil des faisceaux transmis et de la rétrodiffusion sont comparées à des mesures faites en laboratoire à 0.63, 1.06 et 10.6 μm sur des nuages de gouttelettes d'eau. L'accord est très bon pour tous les cas étudiés, les contributions des diffusions multiples variant de négligeables à importantes.

DREV R-4422/86 (UNCLASSIFIED)

Research and Development Branch, DND, Canada.
DREV, P.O. Box 8800, Courcelette, Que. G0A 1R0

"Multiple-Scattering Laser Propagation Model and Comparison with Laboratory Measurements"
by L.R. Bissonnette

A multiple-scattering laser propagation model is developed in the form of three simultaneous partial differential equations for the reduced field amplitude, the forward- and the backscattered irradiances. The scattering and diffusion coefficients are defined in terms of Mie functions, and reduction factors are derived to take into account detection at limited fields of view. Solutions for transmitted beam profiles and integrated backscatter are compared with measurements performed on laboratory-generated water droplet clouds at 0.63, 1.06 and 10.6 μm. The agreement is very good for all conditions investigated, ranging from negligible to important multiple-scattering contributions.

DREV R-4422/86 (UNCLASSIFIED)

Research and Development Branch, DND, Canada.
DREV, P.O. Box 8800, Courcelette, Que. G0A 1R0

"Multiple-Scattering Laser Propagation Model and Comparison with Laboratory Measurements"
by L.R. Bissonnette

A multiple-scattering laser propagation model is developed in the form of three simultaneous partial differential equations for the reduced field amplitude, the forward- and the backscattered irradiances. The scattering and diffusion coefficients are defined in terms of Mie functions, and reduction factors are derived to take into account detection at limited fields of view. Solutions for transmitted beam profiles and integrated backscatter are compared with measurements performed on laboratory-generated water droplet clouds at 0.63, 1.06 and 10.6 μm. The agreement is very good for all conditions investigated, ranging from negligible to important multiple-scattering contributions.

DREV R-4422/86 (UNCLASSIFIED)

Research and Development Branch, DND, Canada.
DREV, P.O. Box 8800, Courcelette, Que. G0A 1R0

"Multiple-Scattering Laser Propagation Model and Comparison with Laboratory Measurements"
by L.R. Bissonnette

A multiple-scattering laser propagation model is developed in the form of three simultaneous partial differential equations for the reduced field amplitude, the forward- and the backscattered irradiances. The scattering and diffusion coefficients are defined in terms of Mie functions, and reduction factors are derived to take into account detection at limited fields of view. Solutions for transmitted beam profiles and integrated backscatter are compared with measurements performed on laboratory-generated water droplet clouds at 0.63, 1.06 and 10.6 μm. The agreement is very good for all conditions investigated, ranging from negligible to important multiple-scattering contributions.

DREV R-4422/86 (UNCLASSIFIED)

Research and Development Branch, DND, Canada.
DREV, P.O. Box 8800, Courcelette, Que. G0A 1R0

"Multiple-Scattering Laser Propagation Model and Comparison with Laboratory Measurements"
by L.R. Bissonnette

A multiple-scattering laser propagation model is developed in the form of three simultaneous partial differential equations for the reduced field amplitude, the forward- and the backscattered irradiances. The scattering and diffusion coefficients are defined in terms of Mie functions, and reduction factors are derived to take into account detection at limited fields of view. Solutions for transmitted beam profiles and integrated backscatter are compared with measurements performed on laboratory-generated water droplet clouds at 0.63, 1.06 and 10.6 μm. The agreement is very good for all conditions investigated, ranging from negligible to important multiple-scattering contributions.